Cu-assisted induced atomic-level bivalent Fe confined on N-doped carbon concave dodecahedrons for acid oxygen reduction electrocatalysis

Yan Luo [a], Zeming Tang [a], Guiqiang Cao [a], Da Bi [a], David P. Trudgeon [b], Adeline Loh [b], Xiaohong Li [b], Qingxue Lai [a]* and Yanyu Liang [a]*

[a.] *Jiangsu Key Laboratory of Electrochemical Energy Storage Technologies, College of Materials Science and Technology, Nanjing University of Aeronautics and Astronautics, 29 Jiangjun Ave., Nanjing, 210016 (P. R. China)*

[b.] *Renewable Energy Group, College of Engineering, Mathematics and Physical Sciences, University of Exeter, Penryn Campus, Cornwall TR10 9FE, UK*

Corresponding Author* laiqingxue@126.com; liangyy403@126.com;

Abstract: Atomically dispersed transition metals anchored on N-doped carbon have been successfully developed as promising electrocatalysts for acidic oxygen reduction reaction (ORR). Nonetheless, how to introduce and construct single-atomic active sites is still a big challenge. Herein, a novel concave dodecahedron catalyst of N-doped carbon (FeCuNC) with well confined atomically dispersed bivalent Fe sites was facilely developed via a Cu-assisted induced strategy. The obtained catalyst delivered outstanding ORR performance in 0.5 M H_2SO_4 media with a half-wave potential ($E_{1/2}$) of 0.82 V (vs reversible hydrogen electrode, RHE), stemming from the highly active bivalent $Fe-N_x$ sites with sufficient exposure and accessibility guaranteed by the high specific surface area and curved surface. This work provides a simple but efficient metal-assisted induced strategy to tune the configurations of atomically dispersed active sites as well as microscopy structures of carbon matrix to develop promising PGM-free catalysts for proton exchange membrane fuel cell (PEMFC) applications.

Keywords: acidic media, atomically dispersed active sites, oxygen reduction reaction, bivalent Fe sites

1. Introduction

The scarcity, prohibitive cost and vulnerability to methanol poisoning represent three huge challenges of platinum group metal (PGM) catalysts for oxygen reduction reaction (ORR) in acidic electrolyte, which gravely impede the extensive implementation of proton exchange membrane fuel cell (PEMFCs) technology [1-6]. The recent report has shown that PGM-free catalysts using earth-abundant elements emerge as an attractive alternative to improve the sluggish ORR kinetics and consequently facilitate application in PEMFCs, due to their ability to meet requirements of low-cost and high-activity [7-10]. Up to now, some progresses have been made in transition metal and nitrogen-doped carbon (M-N-C) catalysts, particularly for Fe-N-C catalysts, representing optimal ORR performance in acidic electrolyte [11-23,39-40].Ye et al. have reported a sort of Fe_2 clusters immobilized on N-doped carbon through accurately regulating the number of iron atoms, showing a $E_{1/2}$ of 0.78 V for acid oxygen reduction electrocatalysis [24]. Wang et al have fabricated a novel non-precious metal Fe-N-C catalyst has through pyrolyzing $Fe-g-C_3N_4@C$ precursors, achieving a Fe-N-C composite with an ORR $E_{1/2}$ of 0.75 V in 0.1 M $HClO_4$ [25]. However, the ORR performance in acidic electrolyte is still restricted significantly by the generation of disadvantageous Fe aggregates, such as carbides, nitrides or oxides and heterogeneous morphology with no homogeneous active site in the carbon matrix [3,17]. As a result, there is still an

obvious activity deficiency in current Fe−N−C catalysts to substitute Pt-based catalysts for PEMFC applications.

Hence, an effective methodology via increasing the density and uniformity of Fe-N_x active sites in the carbon matrix is urgently required to significantly improve the ORR activity of Fe−N−C catalysts [3,4]. Recently, metal−organic frameworks (MOFs) instituted by bridging organic ligands and metal atoms have been considered as ideal precursors to cultivate N-doped carbon for diverse energy applications [3,17]. Among them, zinc-based zeolitic imidazolate frameworks (ZIF-8) with N species, large surface areas and abundant pore structure have been identified to be favorable for the synthesis of Fe-N-C electrocatalysts [1,3,4,17,33-36]. Furthermore, previous work has revealed that Fe^{2+} instead of Fe^{3+} is preferred to uniformly substitute Zn^{2+} in ZIF-8 without visible structural distortion, which provides an ideal precursor for fabricating advanced Fe-N-C ORR electrocatalysts [57].

Moreover, atomically dispersed catalysts, namely single-atom catalysts (SACs), have been recently proposed as a kind of preeminent catalytic material, typically comprising of isolated metal single atoms immobilized on a support [26,27]. Accordingly, not only does SACs possess nearly 100% atomic utilization but also provide highly stable and uniform active sites for efficient ORR electrocatalysis [28-32]. For example, Zhang et al. cultivated single-atom Fe catalysts with porphyrin-like MN_4 coordination configurations confined in the micropores of the hierarchically polyporous carbon support, which demonstrated an ORR $E_{1/2}$ of 0.82 V (vs reversible hydrogen electrode, RHE) in 0.1 M H_2SO_4 [33]. Although fast improvement has been made in atomically

dispersed single metal catalyst, how to introduce and construct single-atomic active sites is still a big challenge. Taken together, a facile and feasible method is still required to tune the atomically distributed Fe active configurations in a controllable carbon matrix to significantly improve the ORR performance of Fe-N-C catalysts.

Herein, a Cu-assisted induced strategy was proposed to develop atomically dispersed bivalent Fe-N_x sites immobilized on N-doped carbon of concave dodecahedron (FeCuNC) as an advanced ORR electrocatalyst in acid media [42-44]. The facile strategy takes advantage of a common redox reaction between Fe^{3+} and Cu ($2Fe^{3+} + Cu = Cu^{2+} + 2Fe^{2+}$) in the precursor to form stable bivalent Fe sites for uniform substitution of Zn^{2+} in zinc-based zeolitic imidazolate frameworks (ZIF-8), which guarantees evenly distributed bivalent Fe-N_x sites in the derived N-doped carbon matrix without visible structural distortion resulted by trivalent Fe substitution. Moreover, only when Fe and Cu with specific doping content are co-doped together can the unique concave dodecahedron morphology of the carbon matrix be formed, resulting in a high specific surface area of 1,265.12 $m^2\ g^{-1}$ and pore volume of 1.82 $cm^3\ g^{-1}$ for sufficient exposure and availability of generated Fe–N_x sites. As a result, the obtained FeCuNC catalyst delivered outstanding ORR performance in 0.5 M H_2SO_4 medium with a half-wave potential ($E_{1/2}$) of 0.82 V (vs reversible hydrogen electrode, RHE).

2. Experimental

2.1 Catalyst preparation

Preparation of ZIF-8: 2-MeIM (6.489 g) was dissolved in 200 mL of methanol; then $Zn(NO_3)_2 \cdot 6H_2O$ (2.933 g) in 200 mL of MeOH was rapidly poured into the

aforementioned solution under vigorous stirring for 1 h at room temperature (RT, 295±2K). The prepared precipitates were centrifuged and washed with MeOH three times, and then dried at 60 °C under vacuum for 12 h.

Preparation of FeCu-ZIF-8: Fe content is given in this work in terms of molar percent of Fe versus the total metal (Fe + Cu + Zn) content from 1% to 9% in the synthesis of precursor. Five FeCuNC catalysts were produced with the Fe/Cu/ (Fe + Cu + Zn) molar ratio of 1:0.5:100, 3:1.5:100, 6:3:100, 7.5:3.75:100 and 9:4.5:100, which were named as 1FeCuNC, 3FeCuNC, 6FeCuNC, 7.5FeCuNC and 9FeCuNC, respectively. Definitely, the optimal molar ratio among Fe^{2+}, Cu^{2+} and Zn^{2+} was 7.5: 3.75: 88.75, which referred to the 7.5FeCu-ZIF precursor with 7.5%Fe and 3.75% Cu content (mol%). The preparation process of the 7.5FCu-ZIF was basically akin to that of ZIF-8. Firstly, 2-methylimidazole (6.489 g) was dissolved in 200 mL methanol, labelled as 1#. After that, 15 pieces of copper foil (2×2 cm^2) were eroded with 3 M HCl for 0.5 h, and then cleaned with distilled water as well as MeOH five times. Next, $Zn(NO_3)_2 \cdot 6H_2O$ (2.603g) and $(Fe(NO_3)_3 \cdot 9H_2O)$ (298.8 mg) were successively dissolved in 200 mL MeOH, followed by the addition of 15 pieces of Cu foil under ultrasonic conditions for about 2 h until the orange solution changed to light green one and remained the same, labelled as 2#. Subsequently, solution 2# was poured into solution 1# rapidly under magnetic stirring for 1 h at RT. At last, the remaining synthesis processes were identical with that of ZIF-8 mentioned above. The contrast sample Fe-ZIF(III) and Cu-ZIF were obtained following the alike crafting processes, just with the addition of proportionate $Zn(NO_3)_2 \cdot 6H_2O$ and $(Fe(NO_3)_3 \cdot 9H_2O)$ or $(Cu(NO_3)_2 \cdot 3H_2O)$,

respectively.

Synthesis of Fe-ZIF(II)-8: Firstly, 2-methylimidazole (6.489 g) was dissolved in 200 mL methanol, labelled as 1[#]. After that, iron powder (15 mg) was eroded with 3 M HCl for 0.5 h, centrifuged and cleaned with distilled water as well as MeOH five times. Next, $Zn(NO_3)_2 \cdot 6H_2O$ (2.713 g) and $(Fe(NO_3)_3 \cdot 9H_2O)$ (199.79 mg) were successively dissolved in 200 mL MeOH, followed by ultrasound with the centrifugally collected iron powder for about 1 h until the orange solution changed to reseda and remained the same, labelled as 2[#]. Subsequently, solution 2[#] was poured into solution 1[#] rapidly under magnetic stirring for 1 h at RT. At last, the remaining synthesis processes were identical with that of ZIF-8 mentioned above.

Synthesis of FeCuNC: FeCu-ZIF crystal precursors were heat-treated at a wide temperature range from 600 to 1100 °C with a rate of 3 °C min^{-1} under Ar flow for 1 h in a tube furnace and naturally cooled to RT to gain the representative FeCuNC electrocatalysts. No additional acidic leaching or second heating treatment were required. The contrast sample FeNC(II), FeNC(III), CuNC, and NC were acquired through the same thermal treatment of Fe-ZIF(II), Fe-ZIF(III), Cu-ZIF, and ZIF-8.

2.2 Characterization

The morphology and structure of these obtained materials were analyzed by Scanning electron microscopy (SEM, ULTRA-55), transmission electron microscopy (TEM, JSM-2100), high-resolution TEM (HRTEM, Philips Tecnai G2), and atomic resolution aberration-corrected high-angle annular dark field scanning transmission electron microscopy (HAADF-STEM, FEI Titan G2 60-300). The other physical

properties of the samples were examined by X-ray diffraction (XRD, ULTRA-55 D5000, Cu Kα), Raman spectra (Lab-RAM HR800), Brunauer–Emmett–Teller measurement (BET, Micrometrics ASAP2020 analyzer at 77 K) and X-ray photoelectron spectroscopy (XPS, Kratos AXIS Ultra spectrometer). The mass content of metal was measured with ICP optical emission spectrometer (Varian 720-ES).

2.3 Electrochemical measurement

All electrochemical measurements were tested in 0.5 M H_2SO_4 (0.1 M $HClO_4$ for 30% Pt/C) at RT on a CHI760D electrochemical workstation assembled with a three-electrode system. A glassy carbon rotating disk electrode (RDE) and rotating ring-disk electrode (RRDE) electrode were used as the working electrode. $Hg/HgSO_4$ (K_2SO_4 - sat., 0.652 saturated V vs. RHE) electrode and a platinum sheet were employed for the reference electrodes in acids and counter electrodes, respectively. 2.0 mg of pulverous catalyst was mixed with 1.0 mL 0.05 wt.% Nafion ethanol solution to produce an ink that was drop-casted onto the RDE or RRDE and air-dried at RT. The loading of catalyst was controlled at 0.5 mg cm^{-2} for all measurements. Then, to determine the electrocatalytic activity for the ORR, Linear sweep voltammetry (LSV) was employed in O_2- or N_2-saturated 0.5 M H_2SO_4 solution with a scan rate of 50 mV s^{-1}. RDE and RRDE tests of ORR were conducted in O_2-saturated 0.5 M H_2SO_4 solution at different rotation speeds with a scan rate of 10 mV s^{-1}. Chronoamperometric curves of ORR were carried out in O_2-saturated 0.5 M H_2SO_4 solution with a rotation speed of 900 rpm at half-wave potential (vs. RHE). The electrode potential was calibrated according to the equation: E (RHE) = E ($Hg/HgSO_4$) + 0.652 + 0.0591*pH.

As for RRDE test, the H_2O_2 yield and n of catalysts were calculated from the following equations:

$$H_2O_2(\%) = 200 \times \frac{I_R/N}{(I_R/N)+I_D}$$

$$n = 4 \times \frac{I_D}{(I_R/N)+I_D}$$

Where I_D is disk current and I_R is ring current; N is ring collection efficiency (0.37).

3. Results and discussion

The preparation process of catalysts is located in the experimental section. A series of catalysts, including non-metal (NC), mono-metal (FeNC(II), FeNC(III), CuNC) and different content and heat treatment temperature of bimetallic (FeCuNC) doped nanocarbon based catalysts, have been synthesized for morphology and activity control. In the specific synthesis process of FeCu-ZIF-8, tetra-coordinated Fe^{2+} with the assistance of Cu is in-situ introduced for partial substitution of Zn^{2+} to form uniformly distributed tetrahedral Fe-N$_4$ configurations in the ZIF-8 nanocrystals. During this process, the incorporation of Cu can efficiently avoid evident structural disorder from the hexa-coordinated configuration of Fe^{3+} coordination [57-59]. The subsequent one-step pyrolysis at a high temperature of 1100 °C is vital for directly transforming bivalent Fe-doped ZIF nanocrystal complexes into atomically dispersed bivalent Fe-N$_x$ embedded nanocarbon based catalysts (FeCuNC). The high-temperature thermal activation process above 907°C can completely remove inert metal Zn, thus leading to high-surface-area structures, which is conducive to provide rational space for creating atomically dispersed bivalent Fe-N$_x$ sites as well their full exposure and utilization. No

additional post-treatment is required in this facile strategy.

Catalyst morphology and structure. The morphology and structure of prepared FeCuNC and other control samples are systematically characterized by SEM, TEM, HRTEM, HADDF-STEM, XRD and BET measurement. It could be found that only the overall morphology of Fe and Cu co-doped catalyst (7.5FeCuNC) is an evenly-distributed concave dodecahedron structure of the carbon matrix (Fig 1D), which is quite different from that of NC with a collapse morphology (Fig 1A, Fig S1 and S2A) and mono-metal doped catalysts (FeNC(II), FeNC(III) and CuNC) with the irregular truncated polyhedral shape (Fig S1B-D, Fig S2B-D). The above results demonstrate that the incorporation of Fe and Cu into the Fe-ZIF-8 framework can promote the generation of unique concave dodecahedron morphology. But it's not an arbitrary amount of Fe and Cu doping can this unique morphology take shape. So, it's vital to set forth the impact of Fe and Cu doping content on the catalyst morphology. The fused morphology (Fig 1B, Fig S3A) without separated particles is found in the 3FeCuNC catalysts on account of inadequate metal content. The nanoparticles begin to separate gradually and the unconspicuous concave structures appear in 6FeCuNC catalysts (Fig 1C, Fig S3B). As the content of Fe and Cu increase, a sort of concave even-distributed dodecahedron shape comes into being in the 7.5FeCuNC catalysts (Fig 1D, Fig S3C), and what matters is that the unique shape allows more exposure of active sites [41]. While keeping up enhancing Fe and Cu content, we have observed that the particle size of 9FeCuNC increases to 200 nm as well as the concave structure is vanished (Fig 1E, Fig S3 D). As a result, we can conclude that only when Fe and Cu with specific doping

content are co-doped together (7.5FeCuNC) can the unique concave dodecahedron morphology of the carbon matrix be formed. And the reliability of the foregoing conclusion is proved by repeated experiments. The concave morphology is generated mainly due to anisotropic thermal shrinkage induced on ZIF-8 rhombohedral surfaces and edges during the carbonization process [41]. The XRD pattern of 7.5FeCu-ZIF-8 matches the pattern of pure ZIF-8 well (Fig 1F), indicating that the introduction of Cu in the precursor helps to maintain the zeolite-type structure and favorable Zn/Fe coordination environment [48,49]. Compared with the NC catalyst, no metal-based crystalline peaks are detected in the XRD pattern of 7.5FeCuNC (FeCuNC described below refers to 7.5FeCuNC) doped with Fe and Cu (Fig 1F, Fig S4), probably due to complete coordination of Fe/Cu with N to form atomically dispersed $Fe-N_x$ and $Cu-N_x$ active sites towards boosted ORR performance [50,51].
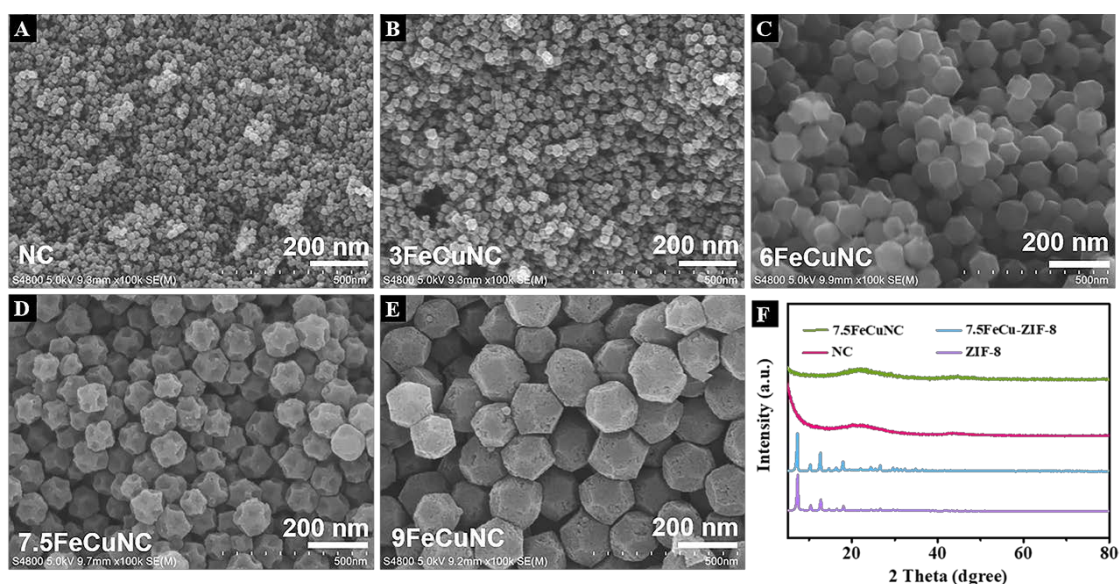

Fig. 1 SEM images of A) NC, B) 3FeCuNC, C) 6FeCuNC, D) 7.5FeCuNC, E) 9FeCuNC and I) XRD patterns of ZIF-8, 7.5FeCu-ZIF-8, NC, and 7.5FeCuNC.

The uniformly distributed concave dodecahedron structure of FeCuNC catalyst is

also shown in the TEM images (Fig 2A, B). The HRTEM images further display that there are no any discernible metal particles in the concave dodecahedrons (Fig 2C, D), which is coincided with XRD patterns above. More critically, the FeCuNC catalysts are abundant in atomically dispersed Fe sites immobilized in the carbon substrate (white lightspot), as confirmed by HAADF-STEM images (Fig 2E). The EDS elemental mapping image in Figure 2F shows the uniform distribution of Fe, Cu, N and C elements in the whole sample. The formation of atom-dispersed Fe sites in FeCuNC can increase the atomic utilization and provide highly stable and uniform active sites for efficient ORR electrocatalysis [28]. The surface area and porous structures of FeCuNC and NC catalysts are investigated by N_2 adsorption–desorption isotherms. Both FeCuNC and NC catalysts reveal type IV isotherms containing hysteresis loops (Fig 2G), mostly on account of the existence of mesopores that are able to enhance mass transport [52]. According to BET measurement (Table S1), the surface area and pore volume of FeCuNC are characterized as 1,265.12 m² g^{-1} and 1.82 cm³ g^{-1}, both of which exceed those of NC (1,016.71 m² g^{-1} and 1.48 cm³ g^{-1}). The greater surface area and micropore volume (0.39 cm³ g^{-1}) of FeCuNC with peculiar concave surface could promote more exposed active sites. On the basis of the pore size distribution plots, such concurrent microporous and mesoporous structures co-exist in the carbon matrix, providing a highly open and hierarchical skeleton to facilitate ORR electrocatalysis (Fig 2H). Combined with experimental results and literature research [1], it can be speculated that such a unique characteristic concave morphology in FeCuNC is significantly beneficial to improve the specific surface area and pore volume for

exposing more reactive sites and enhancing mass transport during ORR electrocatalytic process.
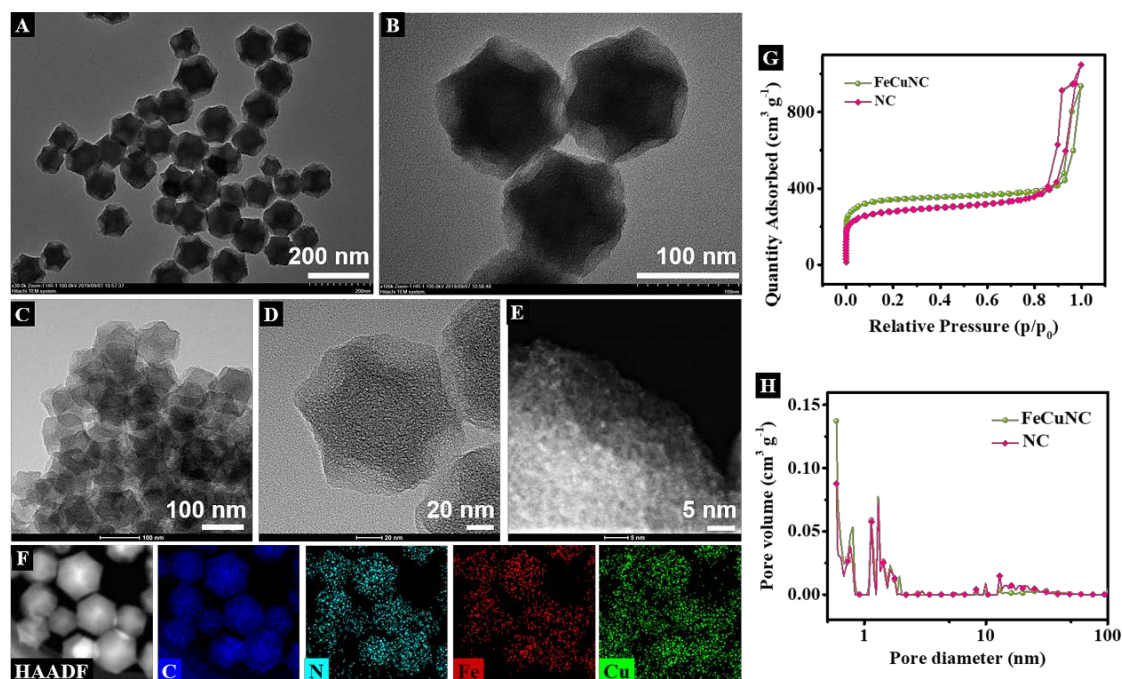

Fig. 2 TEM images of A, B) FeCuNC; High-resolution C, D) TEM images; E) HAADF-STEM image; F) bright-field HAADF-STEM images of FeCuNC with corresponding element mapping images; G) N_2 adsorption–desorption isotherms and H) pore size distribution plots of NC and FeCuNC.

Catalyst performance for the ORR. The ORR performance of obtained electrocatalysts is investigated in 0.5 M H_2SO_4 by RDE experiments [45-47,60]. As shown in Fig 3A, the FeCuNC exhibits prominent electrocatalytic performance comparable with 30% commercial Pt/C [33], which reveals an $E_{1/2}$ of 0.82 V (vs RHE) and an excellent diffusion-limited current density (-5.52 mA cm^{-2}). Besides, the ORR activity of FeCuNC is superior to that of most nonprecious catalysts in acidic media in literature [S1-16] (Table S2). Purely N-doped porous carbon (NC) and mono-metal N-

doped porous carbon (FeNC(II), FeNC(III) and CuNC), in contrast, show a relatively poor activity for ORR (Fig 3A). According to the calculation, the Tafel slope of FeCuNC is 65 mV dec^{-1}, lower to those of Pt/C, FeNC(III), NC, FeNC(II) and CuNC, which demonstrates that the FeCuNC catalyst possesses desirable ORR dynamics (Fig 3B). In short, the ORR performance of above catalysts follows the sequence: FeCuNC > FeNC(II) > FeNC(III) > NC > CuNC (Table S2).

To obtain the most active FeCuNC catalyst, we have further optimized the catalysts by changing Fe doping content (the molar ratio of Cu is a half that of Fe). The activities of FeCuNC catalysts produced by using different Fe doping content (Fig S5) are maximized for 7.5FeCuNC. The NC sample that is not doped with Fe and Cu exhibits poor performance similar to previously reported "metal-free" electrocatalysts [17]. This phenomenon indicates that the catalytic effect of residual Zn in samples on ORR in acidic media can be ignored. With the addition of Fe doping amounts up to to 7.5%, the electrocatalytic performance increases unceasingly, indicating that the introduced Fe-N$_x$ active sites with high density are able to greatly improve the ORR catalytic performance. Nevertheless, further increase of the Fe content to 9% results in a reduced ORR catalytic activity. According to the experimental results, the 7.5FeCuNC catalyst is the best performing composition. Fe and Cu doping content less than optimum value causes the catalysts to produce inadequate active sites, while the catalysts containing higher content of Fe and Cu generate less defects and porosity [17]. The 7.5FeCuNC with the optimal Fe and Cu doping content has the unique concave dodecahedron morphology, which is beneficial to increase the specific area and expose

more atomically dispersed active sites towards the best ORR performance. To obtain the optimal pyrolysis temperature, the influence of pyrolysis temperatures ranging from 700 to 1200 °C on ORR catalytic performance of 7.5FeCuNC is also evaluated (Fig 3C). The electrochemical results indicate that 800 °C is the lowest temperature to activate FeCu-ZIF-8 precursors, and the ORR performance of FeCuNC exhibits a rising trend with the increase of pyrolysis temperature until 1100 °C, among which the generation of more active sites with higher intrinsic activity may be promoted [4]. Nevertheless, when the pyrolysis temperature reaches 1200 °C, the ORR activity shows an obvious downtrend which may be due to the reduction of Fe-N_x sites at high temperature. Thus, 1100 °C can be proved as the most appropriate for thermal decomposition of relevant precursors.

To further evaluate electron transfer number (n), RDE measurements are performed across a range of rotational speeds. The recorded LSV curves of 7.5FeCuNC at various rotation speeds from 400 to 2025 rpm in Figure S6 show a rapidly enhanced diffusion current densities with increasing rotational rates. During the rotation disk electrode test, the increase of rotation rate is conducive to enhancing the rate of oxygen diffusion, which hence increasing the mass transfer rate and finally leading to the increase of limiting current density [53,54]. Furthermore, corresponding Koutecky-Levich (K-L) diagrams (inset of Fig S6) at different electrode potentials display good linearity. The number of transferred electrons calculated according to K-L equation is 3.96, suggesting a four-electron process with first-order reaction kinetics. RRDE experimentation is conducted to illuminate the favorable ORR activity and four-

electron selectivity accurately. As a result, the first-rank FeCuNC electrocatalyst generates a negligible H_2O_2 yield (below 2.5%) within a voltage range from 0.2 to 0.8 V (Fig S7), lower than other samples, indicating minimal side reactions during ORR process. Moreover, the average electron transfer number observed by the RRDE measurements is 3.98, consistent with the result calculated by K-L equation and superior to the other catalysts (Fig 3D). These results indicate that the FeCuNC catalyst possesses high ORR catalytic efficiency.

In order to prove that the catalytic oxygen reduction is a one-step $4e^-$ process, rather than a $2e^- + 2e^-$ pathway. We vary the catalyst loadings within a wide range from 0.2 to 0.5 mg cm^{-2}, the H_2O_2 yields remaining at a very low level (less than 4%) and all of the electron transfer numbers exceed 3.92 (Fig 3E and S8), which can fully prove the one-step $4e^-$ ORR process. In addition, the durability and the methanol resistance of FeCuNC are investigated by chronoamperometry. The stability of FeCuNC catalyst is better than that of 30% commercial Pt/C, FeNC, CuNC and NC catalysts after 12000 s in acidic media (Fig 3F). In the chronoamperometric measurements, after 2% (volume ratio) methanol is injected to acidic electrolyte, the current on FeCuNC holds steady, however, the current on 30% Pt/C drops almost to zero (Fig S9). Accordingly, the FeCuNC catalyst also exhibits admirable tolerance to methanol.
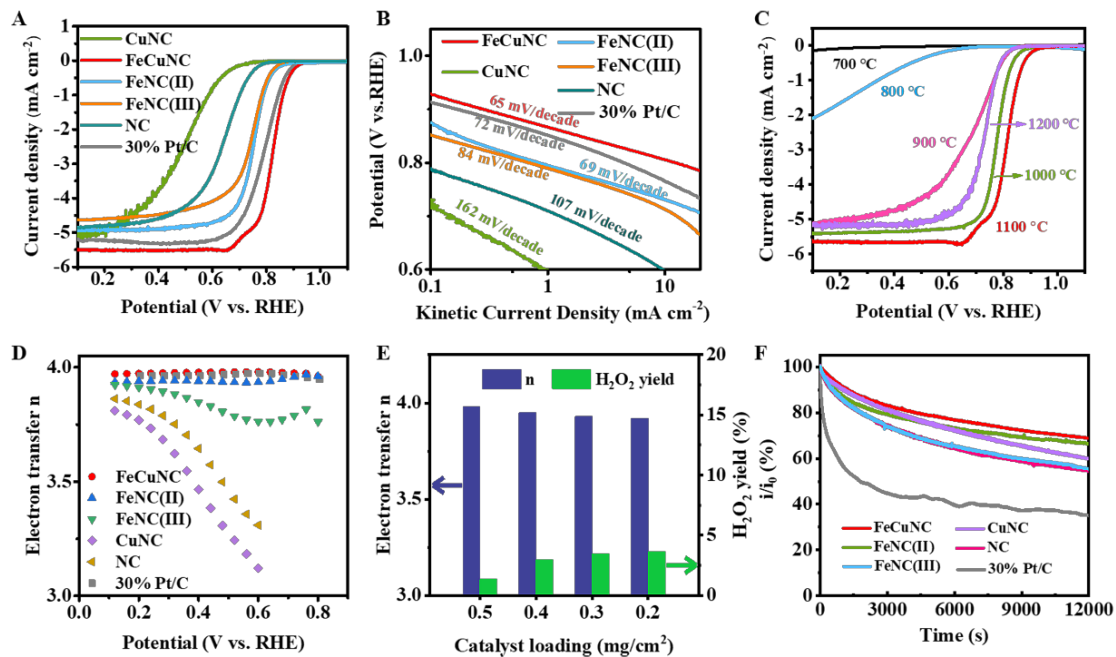
Fig. 3 Electrocatalytic ORR performance in acid media for prepared NC, CuNC, FeCuNC, FeNC(II), FeNC(III) catalysts, and commercial 30% Pt/C: A, B) Comparison of LSV curves and Tafel plots; C) LSV curves of prepared FeCuNC catalysts under different pyrolysis temperature; D) n for prepared catalysts; E) H_2O_2 yield and n depending on different catalyst loading of FeCuNC; F) Stability evaluation of for prepared catalysts.

Elucidation of activity enhancement mechanism. To understand the underlying mechanism of the Cu-assisted induced strategy leading to the optimal activity, we systematically explored the structure−property relationship of the series of catalysts by using XPS analysis and Raman Spectra. These prepared samples are analyzed by XPS to reveal the true active configurations. In the high-resolution Fe 2p XPS spectrum of FeCuNC, five peaks at 711.2, 714.9, 720.8, 724.8 and 728.2 eV (Figure 4A) are corresponding to Fe^{2+} $2p_{3/2}$, Fe^{3+} $2p_{3/2}$, satellite peak, Fe^{2+} $2p_{1/2}$, and Fe^{3+} $2p_{1/2}$, severally, indicating that Fe species exist as Fe^{2+} and Fe^{3+} in the form of Fe-N (Fig 4B). The Fe^{2+} /Fe^{3+} peak area ratios of FeCuNC and FeNC(II) are calculated to be 2.4 and

2.2, apparently higher than that of FeNC(III) (1.0) (Fig 4C). This proves that the content of Fe^{2+} in FeCuNC or FeNC(II) samples are of distinct improvement, suggesting that the incorporation of metallic Cu and Fe could promote the formation of stable bivalent Fe^{2+}-based active sites. According to literature [57-59], not only are the ion radii of Fe^{2+} and Zn^{2+} close (cation radius: Zn^{2+} 60 pm and Fe^{2+} 62 pm), but their stability constants with 2-methylimidazole are also quite similar. In consequence, Fe^{2+} and imidazole ligands could constitute tetra-coordinated $Fe-N_4$ structures, analogous to that of $Zn-N_4$. Whereas the apparently lesser radius (49–55 pm) of Fe^{3+} employs hexa-coordinated structure in imidazole complexes, leading to evident structural disorder in ZIF-8. The ORR activity of FeCuNC and FeNC(II) is much better than FeNC(III), which is due to higher levels of bivalent Fe species in FeCuNC and FeNC(II). The XPS results well confirm our design idea that bivalent Fe plays a fundamental role in enhancing ORR activity. Furthermore, the FeCuNC catalyst shows significantly better ORR property than the FeNC(II), which further suggests the important influence of the Cu on ORR performance improvement of FeCuNC catalyst.

In the high-resolution N 1s XPS spectra of FeCuNC, NC, FeNC(II), FeNC(III) and CuNC(Figure 4B and S10). The N 1s XPS spectrum of all samples can be deconvolved in four peaks at 398.6, 399.4, 401.1 and 403.5 eV, attributed to pyridinic N, M-N (Fe-N/Cu-N. It's not in NC), graphitic N and oxidized N, respectively [38]. The absence of pyrrolic N could be caused by its instability at a high temperature of 1100 °C [37]. Besides, the N doping content of different samples determined using XPS are summarized in Figure 4C, D and Table S3-4. The most active FeCuNC catalyst

possesses the highest total N content. Graphic N and pyridinic N are dominant in all samples. Graphic N can stabilize the geometric structures of carbon, while pyridinic N primarily provides a coordination site with the Fe/Cu to form the atomically dispersed M-N_x sites. According to the bar chart in in red of Figure 4D, the FeCuNC catalyst has the highest M-N content among the four samples, suggesting that the introduction of Cu could induce the increasing content of Fe-N/Cu-N active sites. In the Cu $2p_{3/2}$ spectrum of CuNC catalyst (Fig S11), two deconvoluted peaks at 935.0 eV and 932.9 eV are assigned to Cu(II)-O/N_x and Cu(0) species, indicating the coexistence of Cu nanoparticles and Cu-N bonds in CuNC sample. And the results are consistent with the XRD pattern (Fig S4). The Cu of FeCuNC material is coordinated with nitrogen in the form of Cu-N and does not exist on the surface of the sample, so it couldn't be detected by XPS tests. However, ICP optical emission spectrometry (Table S5) confirms the existence of Cu, as determined from the analysis results, the Fe content in FeCuNC is 2.0 wt.% while Cu content is 0.78 wt.%. Likewise, the EDS elemental mapping image proves that Cu elements are uniformly distributed in the whole sample (Fig 2F). The XPS after the reaction is measured to assist in proving the attribution of the active site. As shown in Figure S12, the M-N content (17.3%) after the reaction is close to that (19%) before the reaction (Fig 4D), which contributes to the attribution of Fe-N/Cu-N active sites throughout the oxygen reaction. And the different types of nitrogen contents of FeCuNC before and after the reaction are very close (Table S6). As a result, FeCuNC catalyst with the best ORR performance actually possesses the highest ratio of Fe-N/Cu-N configurations, indicating the significance of atomically dispersed bivalent Fe-

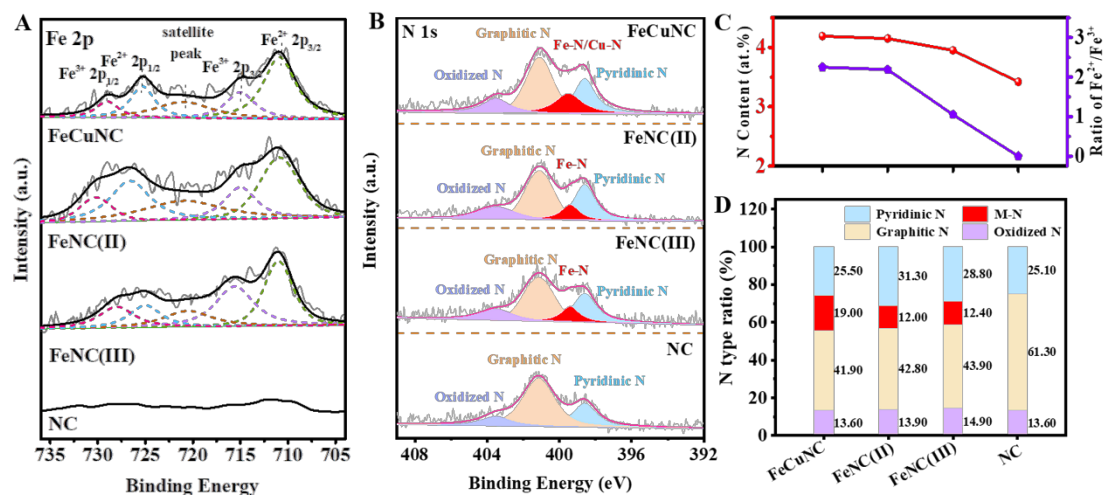$N_x/Cu-N_x$ active sites for oxygen reduction electrocatalysis.

Fig. 4 XPS analysis of FeCuNC, FeNC(II), FeNC(III), and NC: A, B) Fe 2p and N 1s spectrum; C) Comparison of different N doping level as well as atomic ratio of Fe^{2+}/Fe^{3+}; D) Comparison of the content distribution of different typed N sites.

Raman spectra is used to study the carbon structure of FeCuNC catalysts, as compared to the NC, FeNC(II) and FeNC(III) catalyst. There are two dominant signal peaks at around 1360 cm^{-1} (D1) and 1595 cm^{-1} (G) in the Raman spectra of all samples (Fig 5A), corresponding to the sp^3-hybridized disordered carbon and sp^2-hybridized ordered graphite carbon, respectively [55,56]. Moreover, two extra broad peaks at around 1504 cm^{-1} (D2) and 1190 cm^{-1} (D3) can be deconvolved within the whole spectra as well (Fig 5A). They are related to heteroatoms in graphene-sheet structures (D2) and carbon atoms outside of an intact graphene plane (D3), also referred to as heteroatomic defects (D2-type defect) and edge defects (D3-type defect) [55,56]. The D2 peak content (16.34%) of FeCuNC catalysts is higher than that of other control samples, strongly suggesting that the doping of Fe and Cu increases the content of heteroatom-involved carbon defective structures (Fig 5C). Such an important change is probably

due to the formation of Fe-N$_x$/Cu-N$_x$ configurations between two edges of carbon layers to create more Fe/Cu, N-involved carbon defects. As a result, it could be discovered that the highest ratio of D2-type heteroatomic defect involved with Fe-N$_x$/Cu-N$_x$ configurations in FeCuNC makes for the optimal ORR activity (Fig 5B). In addition, the content of D3-type carbon edge defects for FeCuNC (5.12%) is inferior to that of NC (7.69%), which is owing to the much smaller grain size of NC. What's more, the Raman after the reaction is measured to further assist to prove the attribution of the active site. As shown in Figure S14, the D2 peak content (16.4%) of FeCuNC catalysts after the reaction is very close to what it was before the action (16.34), which strongly suggest that the Fe/Cu, N-involved carbon defects sites are stable during the reaction and are in favor of ORR. Based on XPS and Raman spectra results, it could be strongly demonstrated that heteroatomic defect involved with Fe-N$_x$/Cu-N$_x$ configurations in FeCuNC materials makes for the best ORR property.
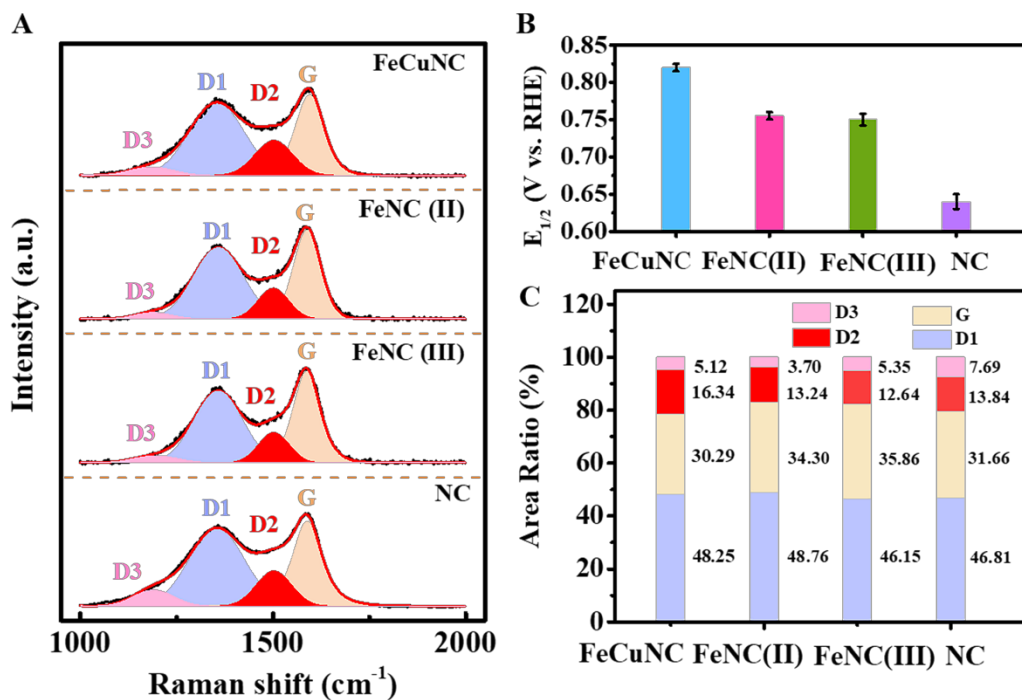
Fig. 5 A) Raman spectra, B) the ORR $E_{1/2}$ and C) the ratio of different C structures of FeCuNC and other control samples.

Through the above electrochemical and physical characterization analysis, it could be well proven that the FeCuNC catalyst exhibits excellent electrocatalytic ORR activities. In short, the high performance is ascribed to the following elements:

1) The unique concave dodecahedron structure endows FeCuNC catalysts with large surface area and hierarchical porous architecture, allowing more exposures of active sites and promoting the mass-transfer;

2) Cu promotes the reduction of Fe^{3+} to Fe^{2+} and forms tetra-coordinated bivalent FeN_4 structure in the derived N-doped carbon matrix without visible structural distortion resulted by trivalent Fe substitution;

3) The introduction of Cu could induce the increasing content of atomically dispersed bivalent $Fe-N_x$ active configurations with high intrinsic activity [4], which is of great significance for ORR electrocatalysis.

4. Conclusions

In conclusion, this work presents a concise approach to prepare a Cu-assisted construction of bivalent Fe-doped ZIF-derived nanocarbon catalyst followed by one-step thermal activation. The unique concave dodecahedron morphology of FeCuNC catalyst is created by a combination of interaction between Fe and Cu with accurate doping content, the appropriate temperature and anisotropic thermal microstress. Compared with Pt/C and other M-N-C catalysts, atomically dispersed bivalent Fe-N_x sites enriched N-doped carbon achieves an outstanding activity and methanol resistance ability for ORR in acidic solution. Notably, the Cu-assisted method has huge merits in construction of atomically dispersed transition M-N_x active sites and well regulation of catalyst morphology. This work furnishes newfangled insights into the reasonable construction and design of cost-effective, high-powered and anti-toxic non-noble metal electrocatalysts with atomically dispersed active sites for ORR electrocatalysis.

Declaration of competing interest

The authors declare that they have no known competing financial interests or personal relationships that could have appeared to influence the work reported in this paper.

Acknowledgements

References

[1] Wang, J. Huang, Z. Liu, W. Chang, C. Tang, H. Li, Z. Chen, W. Jia, C. Yao, T. Wei, S. Wu, Y. Li, Y. Design of N-Coordinated Dual-Metal Sites: A Stable and Active Pt-Free Catalyst for Acidic Oxygen Reduction Reaction. J Am Chem Soc 2017;139:17281-17284.

[2] Kim, C. Dionigi, F. Beermann, V. Wang, X. Moller, T. Strasser, P. Alloy Nanocatalysts for the Electrochemical Oxygen Reduction (ORR) and the Direct Electrochemical Carbon Dioxide Reduction Reaction (CO_2RR). Adv Mater 2019; 31:1805617.

[3] Zhang, H. Hwang, S. Wang, M. Feng, Z. Karakalos, S. Luo, L. Qiao, Z. Xie, X. Wang, C. Su, D. Shao, Y. Wu, G. Single Atomic Iron Catalysts for Oxygen Reduction in Acidic Media: Particle Size Control and Thermal Activation. J Am Chem Soc 2017; 139:14143-14149.

[4] Zhang, H. Chung, H. T. Cullen, D. A. Wagner, S. Kramm, U. I. More, K. L. Zelenay, P. Wu, G. High-performance fuel cell cathodes exclusively containing atomically dispersed iron active sites. Energy Environ Sci 2019;12:2548-2558.

[5] Qiao, Z. Zhang, H. Karakalos, S. Hwang, S. Xue, J. Chen, M. Su, D. Wu, G. 3D polymer hydrogel for high-performance atomic iron-rich catalysts for oxygen reduction in acidic media. Appl Catal B 2017;219:629-639.

[6] Sun, T. Wu, Q. Che, R. Bu, Y. Jiang, Y. Li, Y. Yang, L. Wang, X. Hu, Z. Alloyed Co−Mo Nitride as High-Performance Electrocatalyst for Oxygen Reduction in Acidic Medium. ACS Catal 2015;5:1857-1862.

[7] Liang, Y. Li, Y. Wang, H. Dai, H. Strongly coupled inorganic/nanocarbon hybrid materials for advanced electrocatalysis. J Am Chem Soc 2013;135:2013-2036.

[8] Liang, Y. Li, Y. Wang, H. Zhou, J. Wang, J. Regier, T. Dai, H. Co_3O_4 nanocrystals on graphene as a synergistic catalyst for oxygen reduction reaction. Nat Mater 2011;10:780-786.

[9] Mistry, H. Varela, A. S. Kühl, S. Strasser, P. Cuenya, B. R. Nanostructured electrocatalysts with tunable activity and selectivity. Nat Rev Mater 2016;1:1-14.

[10] Chen, C.-F. King, G. Dickerson, R. M. Papin, P. A. Gupta, S. Kellogg, W. R. Wu, G. Oxygen-deficient $BaTiO_{3-x}$ perovskite as an efficient bifunctional oxygen electrocatalyst. Nano Energy 2015;13:423-432.

[11] Lefevre, M. Proietti, E. Jaouen, F. Dodelet, J. P. Iron-based catalysts with improved oxygen reduction activity in polymer electrolyte fuel cells. Science 2009;324:71-74.

[12] Proietti, E. Jaouen, F. Lefèvre, M. Larouche, N. Tian, J. Herranz, J. Dodelet, J.-P. Iron-based cathode catalyst with enhanced power density in polymer electrolyte membrane fuel cells. Nat Commun 2011;2:1-9.

[13] Gewirth, A. A. Varnell, J. A. DiAscro, A. M. Nonprecious Metal Catalysts for Oxygen Reduction in Heterogeneous Aqueous Systems. Chem Rev 2018;118:2313-2339.

[14] Debe, M. K. Electrocatalyst approaches and challenges for automotive fuel cells. Nature 2012;486:43-51.

[15] Nie, Y. Li, L. Wei, Z. Recent advancements in Pt and Pt-free catalysts for oxygen reduction reaction. Chem Rev 2015;44:2168-2201.

[16] Setzler, B. P. Zhuang, Z. Wittkopf, J. A. Yan, Y. Activity targets for nanostructured platinum-group-metal-free catalysts in hydroxide exchange membrane fuel cells. Nat Nanotechnol 2016;11:1020-1025.

[17] Wang, X. X. Cullen, D. A. Pan, Y. T. Hwang, S. Wang, M. Feng, Z. Wang, J. Engelhard, M. H. Zhang, H. He, Y. Shao, Y. Su, D. More, K. L. Spendelow, J. S. Wu, G. Nitrogen-Coordinated Single Cobalt Atom Catalysts for Oxygen Reduction in Proton Exchange Membrane Fuel Cells. Adv Mater 2018;30:1706758.

[18] Wang, Z. Jin, H. Meng, T. Liao, K. Meng, W. Yang, J. He, D. Xiong, Y. Mu, S. Fe, Cu-Coordinated ZIF-Derived Carbon Framework for Efficient Oxygen Reduction Reaction and Zinc-Air Batteries. Adv Funct Mater 2018;28:1802596.

[19] Wang, T. Sang, X. Zheng, W. Yang, B. Yao, S. Lei, C. Li, Z. He, Q. Lu, J. Lei, L. Dai, L. Hou, Y. Gas Diffusion Strategy for Inserting Atomic Iron Sites into Graphitized Carbon Supports for Unusually High-Efficient CO_2 Electroreduction and High-Performance Zn-CO_2 Batteries. Adv Mater 2020; 32:2002430.

[20] Zheng, W. Yang, J. Chen, H. Hou, Y. Wang, Q. Gu, M. He, F. Xia, Y. Xia, Z. Li, Z. Yang, B. Lei, L. Yuan, C. He, Q. Qiu, M. Feng, X. Atomically Defined Undercoordinated Active Sites for Highly Efficient CO_2 Electroreduction. Adv Funct Mater 2019;30:1907658.

[21] Lei, C. Chen, H. Cao, J. Yang, J. Qiu, M. Xia, Y. Yuan, C. Yang, B. Li, Z. Zhang, X. Lei, L. Abbott, J. Zhong, Y. Xia, X. Wu, G. He, Q. Hou, Y. FeN4 Sites Embedded into Carbon Nanofiber Integrated with Electrochemically Exfoliated Graphene for Oxygen Evolution in Acidic Medium. Adv Energy Mater 2018;8:1801912.

[22] Wang, T. Zhao, Q. Fu, Y. Lei, C. Yang, B. Li, Z. Lei, L. Wu, G. Hou, Y. Carbon-Rich Nonprecious Metal Single Atom Electrocatalysts for CO_2 Reduction and Hydrogen Evolution. Small Methods 2019;3:1900210.

[23] Hou, Y. Qiu, M. Zhang, T. Ma, J. Liu, S. Zhuang, X. Yuan, C. Feng, X. Efficient Electrochemical and Photoelectrochemical Water Splitting by a 3D Nanostructured Carbon Supported on Flexible Exfoliated Graphene Foil. Adv Mater 2017;29:1604480.

[24] Ye, W. Chen, S. Lin, Y. Yang, L. Chen, S. Zheng, X. Qi, Z. Wang, C. Long, R. Chen, M. Zhu, J. Gao, P. Song, L. Jiang, J. Xiong, Y. Precisely Tuning the Number of Fe Atoms in Clusters on N-Doped Carbon toward Acidic Oxygen Reduction Reaction. Chem 2019;5:1-14.

[25] Wang, M.-Q. Yang, W.-H. Wang, H.-H. Chen, C. Zhou, Z.-Y. Sun, S.-G. Pyrolyzed Fe–N–C Composite as an Efficient Non-precious Metal Catalyst for Oxygen Reduction Reaction in Acidic Medium. ACS Catal 2014;4:3928-3936.

[26] Qiao, B. Wang, A. Yang, X. Allard, L. F. Jiang, Z. Cui, Y. Liu, J. Li, J. Zhang, T. Single-atom catalysis of CO oxidation using Pt1/FeOx. Nat Chem 2011;3:634-641.

[27] Chen, F. Jiang, X. Zhang, L. Lang, R. Qiao, B. Single-atom catalysis: Bridging the homo- and heterogeneous catalysis. Chin J Catal 2018;39:893-898.

[28] Yang, H. Shang, L. Zhang, Q. Shi, R. Waterhouse, G. I. N. Gu, L. Zhang, T. A universal ligand mediated method for large scale synthesis of transition metal single atom catalysts. Nat Commun 2019;10:1-9.

[29] Wang, J. Huang, Z. Liu, W. Chang, C. Tang, H. Li, Z. Chen, W. Jia, C. Yao, T. Wei, S. Wu, Y. Li, Y. Design of N-Coordinated Dual-Metal Sites: A Stable and Active Pt-

Free Catalyst for Acidic Oxygen Reduction Reaction. J Am Chem Soc 2017; 139:17281-17284.

[30] Wang, J. Liu, W. Luo, G. Li, Z. Zhao, C. Zhang, H. Zhu, M. Xu, Q. Wang, X. Zhao, C. Qu, Y. Yang, Z. Yao, T. Li, Y. Lin, Y. Wu, Y. Li, Y. Synergistic effect of well-defined dual sites boosting the oxygen reduction reaction. Energy Environ Sci 2018;11:3375-3379.

[31] Xiao, M. Chen, Y. Zhu, J. Zhang, H. Zhao, X. Gao, L. Wang, X. Zhao, J. Ge, J. Jiang, Z. Chen, S. Liu, C. Xing, W. Climbing the Apex of the ORR Volcano Plot via Binuclear Site Construction: Electronic and Geometric Engineering. J Am Chem Soc 2019;141:17763-17770.

[32] Ding, R. Liu, Y. Rui, Z. Li, J. Liu, J. Zou, Z. Facile grafting strategy synthesis of single-atom electrocatalyst with enhanced ORR performance. Nano Res 2020;13:1519-1526.

[33] Zhang, Z. Sun, J. Wang, F. Dai, L. Efficient Oxygen Reduction Reaction (ORR) Catalysts Based on Single Iron Atoms Dispersed on a Hierarchically Structured Porous Carbon Framework. Angew Chem Int Ed 2018;57:9038-9043.

[34] Zhao, L. Wang, A. Yang, A. Zuo, G. Dai, J. Zheng, Y. ZnS, Fe, and P co-doped N enriched carbon derived from MOFs as efficient electrocatalyst for oxygen reduction reaction. Int J Hydrogen Energy 2020: 10.1016/j.ijhydene.2020.08.180.

[35] Du, S. Li, W. Wu, H. Abel Chuang, P.-Y. Pan, M. Sui, P.-C. Effects of ionomer and dispersion methods on rheological behavior of proton exchange membrane fuel cell catalyst layer ink. Int J Hydrogen Energy 2020:10.1016/j.ijhydene.2020.07.241.

[36] Khatib, F. N. Wilberforce, T. Thompson, J. Olabi, A. G. A comparison on the dynamical performance of a proton exchange membrane fuel cell (PEMFC) with traditional serpentine and an open pore cellular foam material flow channel. Int J Hydrogen Energy 2020: 10.1016/j.ijhydene.2020.08.199.

[37] Qiao, Z. Hwang, S. Li, X. Wang, C. Samarakoon, W. Karakalos, S. Li, D. Chen, M. He, Y. Wang, M. Liu, Z. Wang, G. Zhou, H. Feng, Z. Su, D. Spendelow, J. S. Wu, G. 3D porous graphitic nanocarbon for enhancing the performance and durability of Pt catalysts: a balance between graphitization and hierarchical porosity. Energy Environ Sci 2019;12:2830-2841.

[38] Song, L. Wang, T. Li, L. Wu, C. He, J. $Zn_3[Fe(CN)_6]_2$ derived Fe/Fe_5C_2@N-doped carbon as a highly effective oxygen reduction reaction catalyst for zinc-air battery. Appl Catal B 2019;244:197-205.

[39] Chen, A. Kong, A. Fan, X. Yang, X. Li, C. Chen, Z. Shan, Y. High-efficiency copper-based electrocatalysts for oxygen electroreduction by heating metal-phthalocyanine at superhigh temperature. Int J Hydrogen Energy 2017;42:16557-16567.

[40] Sun, M. Li, Z. Liu, Y. Guo, D. Xie, Z. Huang, Q. The synthesis of Fe/NeC@CNFs and its electrochemical performance toward oxygen reaction reduction. Int J Hydrogen Energy 2020; 10.1016/j.ijhydene.2020.08.213.

[41] Wan, X. Liu, X. Li, Y. Yu, R. Zheng, L. Yan, W. Wang, H. Xu, M. Shui, J. Fe–N–C electrocatalyst with dense active sites and efficient mass transport for high-performance proton exchange membrane fuel cells. Nat Catal 2019;2:259-268.

[42] Sun, L. Shi, Z. Wang, H. Zhang, K. Dastan, D. Sun, K. Fan, R. Ultrahigh Discharge

Efficiency and Improved Energy Density in Rationally Designed Bilayer Polyetherimide-BaTiO3/P(VDF-HFP) Composites. J Mater Chem A 2020;8:5750-5757.

[43] Yang, J. Zhu, X. Wang, H. Wang, X. Hao, C. Fan, R. Dastan, D. Shi, Z. Achieving excellent dielectric performance in polymer composites with ultralow filler loadings via constructing hollow-structured filler frameworks. Compos Part A 2020;131:105814.

[44] Sun, L. Shi, Z. Liang, L. Wei, S. Wang, H. Dastan, D. Sun, K. Fan, R. Layer-structured BaTiO3/P(VDF–HFP) composites with concurrently improved dielectric permittivity and breakdown strength toward capacitive energy-storage applications. J Mater Chem C 2020;8:10257-10265.

[45] Fathinezhad, M. AbbasiTarighat, M. Dastan, D. Chemometrics heavy metal content clusters using electrochemical data of modified carbon paste electrode. Environ Nanotechnol Monit Manag 2020;14:100307.

[46] Abbasi, S. Hasanpour, M. Ahmadpoor, F. Sillanpää, M. Dastan, D. Achour, A. Application of the statistical analysis methodology for photodegradation of methyl orange using a new nanocomposite containing modified TiO_2 semiconductor with SnO_2. Int J Environ An Chem 2019:1-17. Int. J. Environ. An. Chem.

[47] Yin, X. T. Dastan, D. Wu, F. Y. Li, J. Facile Synthesis of SnO_2/$LaFeO_3$-XNX Composite: Photocatalytic Activity and Gas Sensing Performance. Nanomater 2019;9:1163.

[48] Dastan, D. Effect of preparation methods on the properties of titania nanoparticles: solvothermal versus sol–gel. Appl Phys A 2017;123:699.

[49] Zhou, W. D. Dastan, D. Li, J. Yin, X. T. Wang, Q. Discriminable Sensing Response

Behavior to Homogeneous Gases Based on n-ZnO/p-NiO Composites. Nanomater 2020; 10:785.

[50] Jafari, A. Tahani, K. Dastan, D. Asgary, S. Shi, Z. Yin, X.-T. Zhou, W.-D. Garmestani, H. Ţălu, Ş. Ion implantation of copper oxide thin films; statistical and experimental results. Surf Interfaces 2020; 18:100463.

[51] Jafari, A. Alam, M. H. Dastan, D. Ziakhodadadian, S. Shi, Z. Garmestani, H. Weidenbach, A. S. Ţălu, Ş. Statistical, morphological, and corrosion behavior of PECVD derived cobalt oxide thin films. J Mater Sci: Mater Electron 2019;30:21185–21198

[52] Dastan, D. Chaure, N. Kartha, M. Surfactants assisted solvothermal derived titania nanoparticles: synthesis and simulation. J Mater Sci: Mater Electron 2017;28:7784-7796.

[53] Lai, Q. Zheng, L. Liang, Y. He, J. Zhao, J. Chen, J. Metal–Organic-Framework-Derived Fe-N/C Electrocatalyst with Five-Coordinated Fe-N$_x$ Sites for Advanced Oxygen Reduction in Acid Media. ACS Catal 2017;7:1655-1663.

[54] Zhao, Y. Lai, Q. Zhu, J. Zhong, J. Tang, Z. Luo, Y. Liang, Y. Controllable Construction of Core–Shell Polymer@Zeolitic Imidazolate Frameworks Fiber Derived Heteroatom- Doped Carbon Nanofiber Network for Efficient Oxygen Electrocatalysis. Small 2018;14:1704207.

[55] Wu, G. Johnston, C. M. Mack, N. H. Artyushkova, K. Ferrandon, M. Nelson, M. Lezama-Pacheco, J. S. Conradson, S. D. More, K. L. Myers, D. J. Zelenay, P. Synthesis–structure–performance correlation for polyaniline–Me–C non-precious

metal cathode catalysts for oxygen reduction in fuel cells. J Mater Chem 2011;21: 11392-11405.

[56] Tuinstra, F. Koenig, J. L. Raman Spectrum of Graphite. J Mater Chem Phys 1970;53:1126-1130.

[57] Wang, X. Zhang, H. Lin, H. Gupta, S. Wang, C. Tao, Z. Fu, H. Wang, T. Zheng, J. Wu, G. Li, X. Directly converting Fe-doped metal–organic frameworks into highly active and stable Fe-N-C catalysts for oxygen reduction in acid. Nano Energy 2016;25:110-119.

[58] Tian, J. Morozan, A. Sougrati, M. T. Lefevre, M. Chenitz, R. Dodelet, J. P. Jones, D. Jaouen, F. Optimized synthesis of Fe/N/C cathode catalysts for PEM fuel cells: a matter of iron-ligand coordination strength. Angew Chem Int Ed 2013;52:6867-6870.

[59] Reichel, F. Clegg, J. K. Gloe, K. Gloe, K. Weigand, J. J. Reynolds, J. K. Li, C. G. Aldrich-Wright, J. R. Kepert, C. J. Lindoy, L. F. Yao, H. C. Li, F. Self-assembly of an imidazolate-bridged Fe(III)/Cu(II) heterometallic cage. Inorg Chem 2014;53:688-690.

[60] Cui, S. Li, M. Bo, X. Co/Mo2C composites for efficient hydrogen and oxygen evolution reaction. Int J Hydrogen Energy 2020;45:21221-21231.